Research Article
Vol. 27, No. 3 | 4 Feb 2019 | OPTICS EXPRESS 3771
Optics EXPRESS

Resonant-cavity infrared detector with five-quantum-well absorber and 34% external quantum efficiency at 4 μm

CHADWICK L. CANEDY,[1] WILLIAM W. BEWLEY,[1] CHARLES D. MERRITT,[1] CHUL SOO KIM,[1] MIJIN KIM,[2] MICHAEL V. WARREN,[3] ERIC M. JACKSON,[1] JILL A. NOLDE,[1] C. A. AFFOUDA,[1] EDWARD H. AIFER,[1] IGOR VURGAFTMAN,[1] AND JERRY R. MEYER[1,*]

[1] *Naval Research Laboratory, 4555 Overlook Ave. SW, Washington, DC 20375, USA*
[2] *KeyW Corporation, Hanover, MD 21076, USA*
[3] *ASEE Postdoctoral Associate Residing at NRL, USA*
**MWIR_laser@nrl.navy.mil*

Abstract: We report resonant-cavity infrared detectors with 34% external quantum efficiency at room temperature at the resonant wavelength of 4.0 μm, even though the absorber consists of only five quantum wells with a total thickness of 50 nm. The full width at half maximum (FWHM) linewidth is 46 nm, and the peak absorption is enhanced by nearly a factor of 30 over that for a single pass through the absorber. In spite of an unfavorable Shockley-Read lifetime in the current material, the dark current density is at the level of state-of-the-art HgCdTe detectors as quantified by "Rule 07." The Johnson-noise limited detectivity (D^*) at 21°C is 7×10^9 cm Hz^{½}/W. We expect that future improvements in the device design and material quality will lead to higher quantum efficiency, as well as a significant reduction of the dark current density consistent with the very thin absorber.

1. Introduction

In a broadband infrared (IR) photodetector, the incident light generates electron-hole pairs by making at most two passes through the absorber. Since the absorption coefficient in a typical midwave-IR (MWIR) material is $\alpha = 2000\text{-}4000\ \text{cm}^{-1}$ at 80% of the bandgap wavelength, the absorber must be at least 3-4 μm thick to produce an internal quantum efficiency > 70%. Since the dark current scales with absorber thickness (if the device is diffusion limited), increasing the thickness to improve the efficiency comes at a cost of higher noise [1,2]. Historically, the lowest dark current densities for MWIR detection have been achieved by bulk HgCdTe photodiodes [3,4], although recently type-II Ga-free III-V superlattices have approached the typical performance levels of HgCdTe [5,6].

However, the close relation between absorber thickness and quantum efficiency is broken if the effective optical path length in the absorber can be increased without making it thicker. One possibility is to diffract the incident light into in-plane-propagating modes, e.g., associated with surface plasmon polaritons supported by a metal film [7,8]. Another is to place the absorber in a resonant cavity that provides multiple passes of the incident light [9]. The resulting resonant cavity infrared detector (RCID) can attain high external quantum efficiency (EQE) at the expense of broadband spectral response. If the RCID is used to sense light from a narrowband source, such as a laser, or when a limited spectral bandwidth is desired as in multispectral or hyperspectral imaging, the sharp spectral response at the resonance wavelength λ_{res} is advantageous because it suppresses background photocurrents at unwanted wavelengths outside the narrow band of interest. The RCID structure may also be beneficial in materials with minority-carrier diffusion length much shorter than the absorption

#353258 https://doi.org/10.1364/OE.27.003771
Journal © 2019 Received 3 Dec 2018; revised 10 Jan 2019; accepted 11 Jan 2019; published 1 Feb 2019

depth, due to very low mobility or very short lifetime, by significantly shortening the distance over which the photogenerated carriers must be collected.

The RCID concept has been studied extensively at shorter wavelengths [9–12], where resonant cavity photodiodes with enhanced frequency response are relatively mature. However, of the MWIR lead-salt or III-V RCIDs reported to date, only one achieved a substantial reduction of the dark current noise combined with high peak quantum efficiency [13–17], and most did not operate at room temperature. The single recent exception was an RCID with 100-nm-thick bulk InAs absorber and resonant wavelength of 2.91 µm [18], for which the resonance enhancement factor and D^* were not presented. Here we report an RCID operating at λ_{res} = 4.0 µm that is designed in accordance with [19]. The entire Ga-free absorber comprises only five type-II "W" quantum wells (QWs) with total thickness 50 nm. An EQE of 34% is obtained with dark current density roughly at the level of "Rule 07" [20], and there is a clear path toward substantial further improvements. Section 2 discusses the RCID design, Section 3 the epitaxial growth and fabrication, and Section 4 the experimental results. Section 5 then offers some conclusions.

2. Design

The key RCID design parameters are the reflectivities of the two mirrors, R_1 and R_2, and the length of the optical cavity L. Assuming weak absorption for a single pass through the absorber with thickness d (i.e., $\alpha d << 1$), the internal quantum efficiency at the cavity's resonant wavelength is [9]:

$$\eta_{max} \approx \frac{\left[1+R_2\left(1-\alpha d\right)\right]\left(1-R_1\right)S\alpha d}{\left(1-\sqrt{R_1R_2}\left(1-\alpha d\right)\right)^2} \tag{1}$$

Here $0 < S < 2$ is the antinode enhancement factor that depends on the overlap of the cavity field and absorber and attains its maximum value when an absorber with $d \to 0$ is placed exactly at the antinode of the field. The present devices employ a 50-nm-thick absorber with five QWs, for which $\alpha d \approx 1.5\%$. Precise placement of this thin absorber within the cavity should lead to $S \approx 1.99$.

Since any light escaping from the back mirror cannot be absorbed, its reflectivity is preferably as high as possible. Whatever its value, the efficiency η_{max} reaches its maximum when $R_1 \approx R_2$. Since the detector also requires a metal contact, it is natural to consider using the contact as a metallic reflector. However, typical contact adhesion layers such as Ti induce a relatively high loss that significantly lowers the reflectivity compared to pure Au or Ag. Therefore, the back mirror employed in the present work consists of an optically thick layer of Ag, followed by Au without any additional adhesion layers. This mirror has an estimated reflectivity $R_2 \approx 96\%$ for light incident from the semiconductor. The optical field has a node near the Ag/semiconductor interface.

Since the front mirror must be positioned between the absorber and the GaSb substrate, it requires the epitaxial growth of a Bragg reflector. This can be challenging, as will be discussed below. The design of the front mirror also affects the spectral bandwidth of the resonance, which narrows dramatically if both reflectivities are high. In general, the full width at half maximum (FWHM) is [9]:

$$\Delta\lambda_{FWHM} \approx FSR\frac{1-\sqrt{R_1R_2}\left(1-\alpha d\right)}{\pi\sqrt{R_1R_2}\left(1-\alpha d/2\right)} \tag{2}$$

where the free spectral range $FSR = \lambda^2_{res}/[2n_{eff}(L + L_{eff,1} + L_{eff,2})]$, n_{eff} is the effective refractive index of the resonant optical mode, and $L_{eff,1}$, $L_{eff,2}$ are penetration depths into the two mirrors [21]. When $R_2 \approx 1$ and neglecting the absorption, Eq. (2) becomes approximately:

$$\Delta\lambda_{FWHM} \approx FSR\frac{1-\sqrt{R_1}}{\pi\sqrt{R_1}} \tag{3}$$

The optical field has a node close to the interface between the lower-index semiconductor that forms most of the cavity (in our devices, the photodiode consisting of the absorber QWs and the associated *n*-type and *p*-type regions) and the first high-index layer of the mirror (GaSb).

Based on these considerations, the absorber should be placed at a distance of $(2m + 1)\lambda_{res}/(4n_{eff})$, where $m = 0,1,2\ldots$, from the metal mirror (including the penetration depth into the metal). Since $\lambda_{res}/(4n_{eff}) < 300$ nm (for $m = 0$) is too thin to include the entire *p* side of the device, we chose a distance of $3\lambda_{res}/(4n_{eff})$ ($m = 1$) to keep the cavity length at $\approx 2\lambda_{res}/n_{eff}$, with a free spectral range of ≈620 nm. For example, R_1 in the 70-90% range leads to a linewidth $\Delta\lambda_{FWHM}$ of several tens of nm. The present Bragg mirror is 7 periods of a GaSb/$AlAs_{0.08}Sb_{0.92}$ quarter-wavelength stack, with an estimated $R_1 \approx 74\%$. Using these reflectivities in Eqs. (1) and (2), we expect $\eta_{max} \approx 52\%$ and $\Delta\lambda_{FWHM} = 40$ nm. All of these calculations assume normal incidence and the presence of a perfect anti-reflection (AR) coating on the substrate surface that the light sees before entering the cavity of the RCID. At larger angles, there is a blue shift of the resonant wavelength, which results in additional broadening and a gradual reduction of the peak EQE. Figure 1 schematically illustrates the entire device structure.

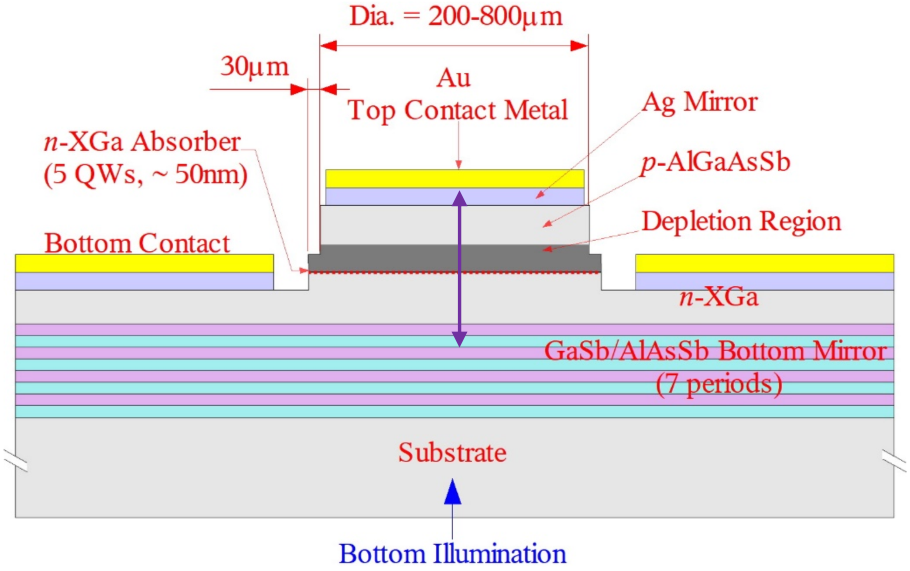

Fig. 1. Schematic of the RCID layer structure and the patterned device geometry.

Figure 2 shows the photodiode heterostructure that fits within the RCID cavity. Starting from the top *p* side of the *p*-*n* junction, there is a 20-nm-thick heavily-doped GaSb contact layer, followed by a *p*-type $Al_{0.5}Ga_{0.5}As_{0.04}Sb_{0.96}$ layer lattice matched to GaSb. This *p*-region with thickness ≈500 nm also serves as a spacer layer whose precise thickness is varied to adjust the cavity length and position of the optical antinode. Below that is a 200-nm-thick undoped AlGaAsSb layer that forms the device's depletion region, where most of the applied bias drops. The limited penetration of the applied field into the absorber allows the device to remain diffusion limited to lower operating temperatures. Below the undoped AlGaAsSb layer is the 5-period 30 Å InAs/20 Å $InAs_{0.5}Sb_{0.5}$/30 Å InAs/20 Å AlSb "W" QW absorber, which is designed for a bandgap wavelength of 4.5 μm. The total absorber thickness of only 50 nm is far smaller than the several μm typically required to obtain high quantum efficiency in the MWIR. The absorber is not intentionally doped, which for similar Ga-free structures leads to electron densities between 10^{15} and 10^{16} cm^{-3}. The absorber is grown on top of a 600-nm-thick wider-gap (E_g = 0.47 eV) 26.4 Å InAs/7 Å $InAs_{0.5}Sb_{0.5}$/26.4 Å InAs/10 Å AlSb “W” superlattice with *n*-type doping graded from 5 × 10^{16} cm^{-3} to 3 × 10^{18} cm^{-3}. Next is the 300-nm-thick heavily *n*-doped $InAs_{0.92}Sb_{0.08}$ contact layer, which is placed at a node of the optical field to minimize free-carrier absorption loss. This is followed by a Ga-free “W” QW spacer layer, which like the top *p*-region has variable thickness to allow adjustment of the cavity thickness and placement of the absorber at the optical antinode. Finally, below this is the 7-period GaSb/AlAsSb Bragg mirror.

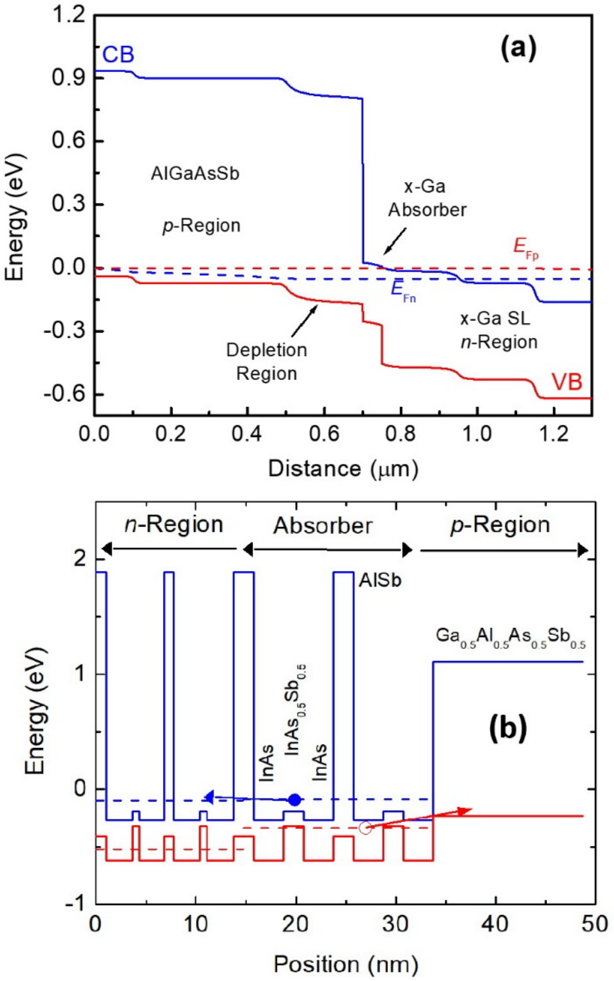

Fig. 2. (a) Band diagram of the RCID structure near the absorber layer, at a bias of −50 mV, (b) Flat-band profiles for the *n*-region, absorber, and *p*-region of the Ga-free photodiode. For simplicity the figure shows only two type-II “W” absorber QWs, whereas the grown structure contains 5 QWs with net thickness 50 nm.

3. Growth and fabrication

The RCID structure described above was grown on a lightly *n*-doped (nearly transparent in the MWIR) GaSb substrate in a Riber Compact 21T molecular beam epitaxy (MBE) system. Removal of the oxide and the buffer layer growth was similar to the procedures described previously [22]. The bottom GaSb/AlAsSb mirror was grown using parameters similar to those in [23]. The core region of the RCID structure including the Ga-free “W” SLs and the AlGaAsSb random alloy layers were grown at a lower temperature than the mirror layers

(~420 °C). The 7-period GaSb/$AlAs_{0.08}Sb_{0.92}$ Bragg mirror stack was grown with the GaSb doped light *n*-type, in order to reduce free-carrier absorption by the background holes that would otherwise be present, while the AlAsSb was not intentionally doped. As described for the previous growth of a GaSb/AlAsSb Bragg mirror for an MWIR interband cascade vertical cavity surface-emitting laser (ICVCSEL) [23], it was necessary to monitor the deposition by optical feedback, to assure sufficient control over the layer thicknesses for maximum reflectivity. In order to calibrate the optical properties of the Bragg mirror, test samples with 5 mirror periods were grown. Adjustments of the growth rate were made to optimize the position of the reflectivity peak, as shown in Fig. 3. We then grew two full device wafers with mirrors (RCIDs I and II) and the same active QW designs, but with slightly adjusted top and bottom spacer thicknesses in the second growth to fine-tune the resonance wavelength. Because these structures were grown shortly after the MBE system was vented for maintenance, the material quality of RCID II improved substantially (as will be seen from the dark current data presented below). Test detector wafers with the same absorber and photodiode configuration but no Bragg mirror were also grown (before the vent) for comparison to the RCIDs. Photoluminescence (PL) measurements were performed on separately grown samples with much thicker (0.5 μm) absorbers. The integrated PL intensity also improved between the first and second RCID growths, although it remained slightly below the best results for test structures grown before the vent. From measurements of the roll-off in optical response with modulation frequency when pumped with a 1064 nm laser, one of the PL structures was determined to have a minority-carrier lifetime of 50 ns at low photoexcited carrier densities.

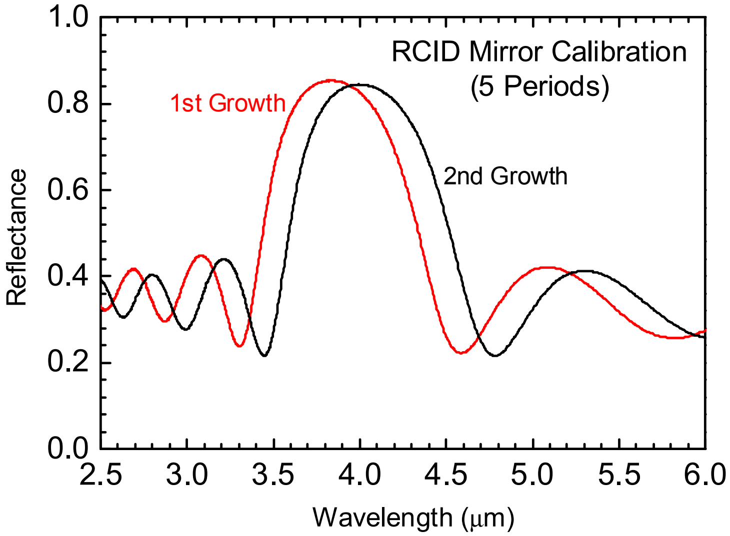

Fig. 3. Experimental reflectance from two 5-period AlAsSb/GaSb Bragg mirrors grown on GaSb substrates. The layer-thickness information deduced from the first growth was used to center the reflectivity of the second mirror at 4.0 μm.

Optical lithography with a two-step wet etch were used to process the devices into circular mesas. First, shallow mesas with diameters of 200, 400, 600 and 800 μm were etched down to just below the *p*-doped AlGaAsSb layer, using an HCl-based etchant. These were then centered on a larger mesa defined by a deep etch that extended all the way to the InAsSb *n*-contact layer, leaving a 30 μm-wide annular "shoulder" around the base of the inner mesa. The deep etch used an HCl-based etchant followed by an H_3PO_4-based etchant. The stepped mesa structure suppresses sidewall leakage across the narrow-gap absorber, by introducing a lateral separation between the sidewalls of the heavily doped *p*-contact and the *n*-type absorber [24]. This was followed by deposition of a 200-nm-thick Ag mirror and a 300-nm-thick Au contact on the top epitaxial surface of the device. The test bar was mounted epitaxial-side-down and illuminated through the substrate. For some of the measurements, an anti-reflection (AR) coating of alumina was also applied to the substrate surface.

4. Results

Figure 4 shows the dark current-voltage (*J-V*) characteristics at room temperature for 800-µm-diameter mesas processed from the two RCID wafers. Results are also shown for a test structure with the same 5-QW absorber, but no bottom mirror to form a cavity. In reverse bias, the dark current density for RCID II is substantially lower, which is consistent with the expectation of higher minority carrier lifetime based on the higher PL intensity. At an applied bias of −60 mV, the dark current densities are 37 mA/cm^2 for RCID II and 26 mA/cm^2 for the test structure. The dark *J-V* characteristics for mesas with different areas are nearly identical, indicating negligible sidewall leakage.

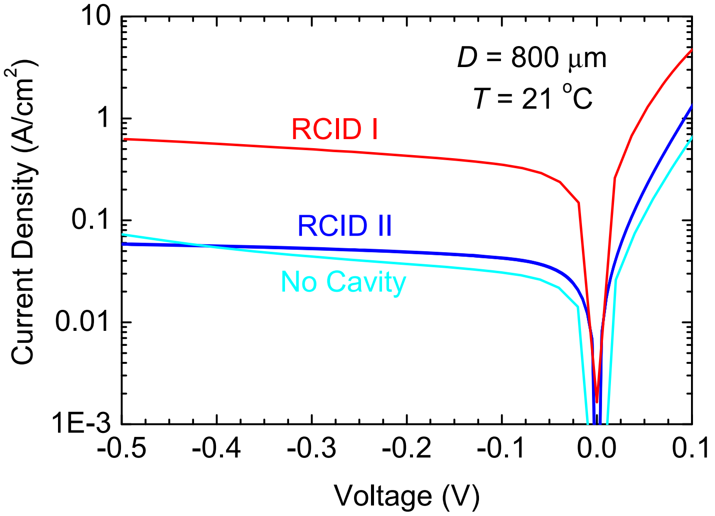

Fig. 4. Dark current density vs. voltage at T = 21 °C for 800-µm-diameter mesas fabricated from both RCID structures, as well as a test structure with no resonant cavity.

Figure 5 shows the dependence of dark current density on temperature for RCID II at a fixed bias of −50 mV. The transport is diffusion limited at $T > 200$ K, with an activation energy of 293 meV that is close to the low-temperature energy gap. At lower temperatures, generation-recombination (G-R) processes, presumably associated with traps in the absorber, come to dominate. The activation energy then drops significantly, to 138 meV. At room temperature, where the diffusion contribution dominates, the *J-V* characteristics are quite consistent from device to device. For example, the dark current densities for 55 devices with all four mesa diameters from the RCID II wafer differ by less than 20% at the operating voltage of −60 mV, with only 4 outliers. However, at 100 K the G-R-dominated dark currents vary much more significantly, with the currents for 48 devices spanning roughly an order of magnitude (with 11 outliers). At 100 K the variation also tends to become greater with decreasing mesa diameter, possibly owing to a non-uniform distribution of traps in the sample.

When the dark current density for an RCID II device is compared at T = 200 K to simulation results from the NRL MULTIBANDS drift-diffusion solver [25], the fit implies a lifetime of ≈10 ns. This is much lower than the lifetimes of up to 2.3 µs that have been reported for state-of-the-art Ga-free detector structures with even narrower energy gaps at the same temperature [6]. The large difference indicates considerable room for improvement in the present RCID performance. The dark current density at room temperature is close to the value expected from “Rule 07” [20], but should be much lower because of the very thin absorber.

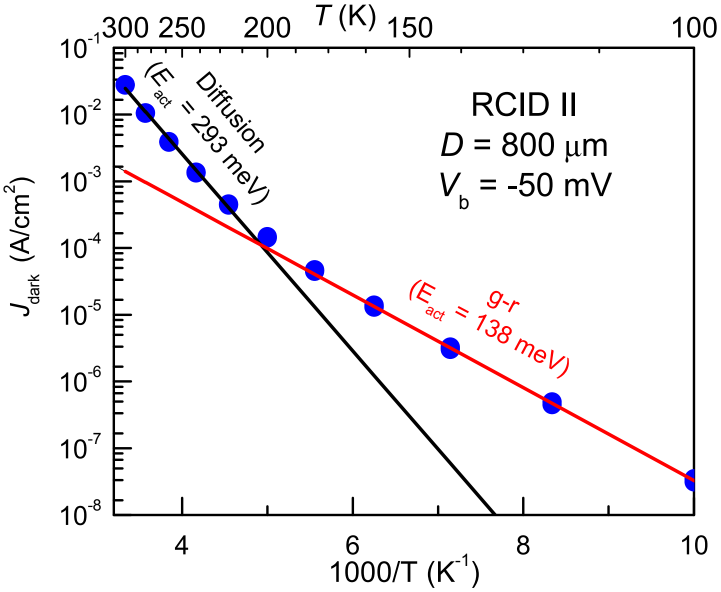

Fig. 5. Dark current density for RCID II as a function of operating temperature at a fixed bias voltage of −50 mV. Also shown are fits to the data above and below 200 K, which yield the indicated activation energies,.

EQEs as a function of wavelength were determined from two measurements. Initially, the relative spectral response was measured with a 1000°C blackbody sourced through a monochromator with 5 nm resolution. The spectral throughput of the monochromator and optics was calibrated using a 5-mm-diameter Gooch and Housego thermal detector with nearly flat spectral response from 1 to 14 µm. While this was adequate to measure the relative EQE normalized to unity at the maximum value, uncertainties in the spot size prevented accurate quantification of the power delivered to the 800 µm diameter device. Next, the photocurrent was measured for a known spectral flux density within a bandwidth containing the peak spectral response. For this measurement, a 1050 °C blackbody was imaged to a 250-µm-diameter spot directly on to the device after passing through a series of filters: a narrow band-pass filter with 150 nm FWHM centered at 4.0 µm, a 2.59 µm long-pass filter, and 5.0 µm short-pass filter. The latter two filtered extraneous transmission of the narrow band-pass filter that may otherwise have affected both the device response and the power calibration. Finally, the scaling factor for the EQE was determined to be consistent with the photocurrent measured for the fixed spectral bandwidth. Figure 6 shows the EQE spectra for RCIDs I and II at 21 °C and an operating bias of −60 mV. Both devices display strong, narrow resonances, although only RCID II is centered at the Bragg mirror reflectance peak near 4.0 µm. Since the semiconductor mirror employed in this work has a limited bandwidth of ≈400 nm, fringes beyond the stop band are also observed. In particular, RCID II displays a long-wavelength feature near the apparent energy gap corresponding to $\lambda = 4.6$ µm, which is 100 nm longer than the design value at room temperature. Measurements of the spectrum for RCID II as a function of temperature show that the peak EQE increases slightly at 200 K, but then decreases at 100 K as the resonance wavelength approaches the band edge. This catchup occurs because the blue shift of the bandgap is more rapid than the blue shift of the resonance wavelength governed by the refractive index.

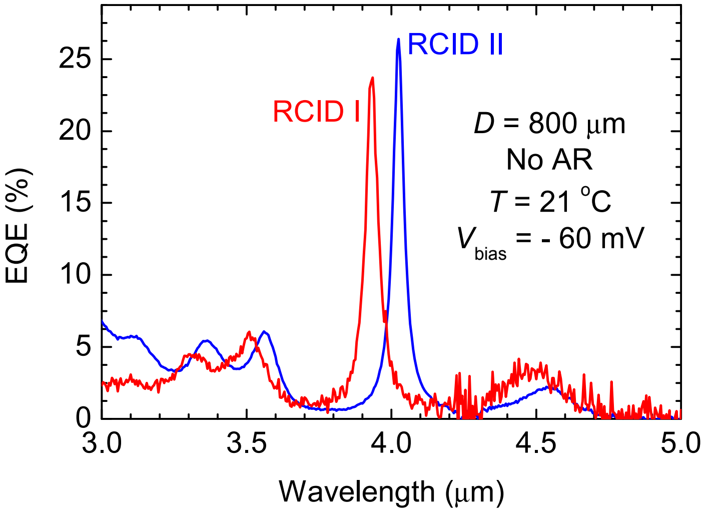

Fig. 6. External quantum efficiency spectra at $T = 21$ °C for both RCIDs with mesa diameters of 800 μm without AR coatings, at the same applied bias of −60 mV.

For a second round of measurements on RCID II, an AR coating consisting of a single layer of alumina was deposited on the substrate side to increase the EQE. Figure 7 shows the resulting spectrum over a narrower range of wavelengths near the resonance. The peak's FWHM is 46 nm, which nearly matches the value calculated in Section 2 when off-normal broadening and the angular field of view of 14° due to the *f*/2 optics are taken into account. We estimate that the maximum EQE of 34% would increase to 38% if all the incident light were collimated at zero angle. However, even with that correction the result is significantly smaller than the value 52% that was estimated from theory in Section 2. Since the resonance width is close to the expected value, a potential source of the discrepancy is imperfect placement of the absorber with respect to the cavity antinode, such that the antinode enhancement factor decreases to $S \approx 1.45$. However, that would require either the distance to the metal mirror or the average index to differ from the simulated values by ≈10%, which appears much larger than estimated uncertainties. Further work is needed to fully reconcile the measured values with theoretical estimates.

For comparison, Fig. 7 also shows the EQE spectrum for the test structure that was grown without a Bragg mirror that could form a resonant cavity. Even though a metal mirror was present, the distance to the mirror was chosen so that it provided almost no net interference-related enhancement or suppression of the EQE at normal incidence. The value near 4.0 μm is 0.9%, and the non-resonant variation with wavelength is of course quite gradual. Comparing this result to the RCID value of 26% without an AR coating indicates that the resonance enhancement factor is nearly a factor of 30. When the QE of 34% realized with an AR coating is combined with the result $R_0A = 0.68\ \Omega\ \text{cm}^2$ from the *J*-*V* characteristics, we obtain a peak detectivity at $T = 21$ °C of $D^* = 7 \times 10^9$ cm Hz$^{1/2}$/W in the limit of zero field of view. By comparison, the best previously reported result for an MWIR RCID operating at room temperature was 7.2×10^8 cm Hz$^{1/2}$/W, for a PbTe-based device with $\lambda_{res} = 3.5$ μm [17]. Commercially available photovoltaic detectors with similar cut-off wavelengths have D^* values in the low-to-mid 10^9 cm Hz$^{1/2}$/W range [26], and $D^* = 1 \times 10^9$ cm Hz$^{1/2}$/W was recently demonstrated for an interband cascade photodetector with a cut-off wavelength of 4.3 μm at room temperature [27].

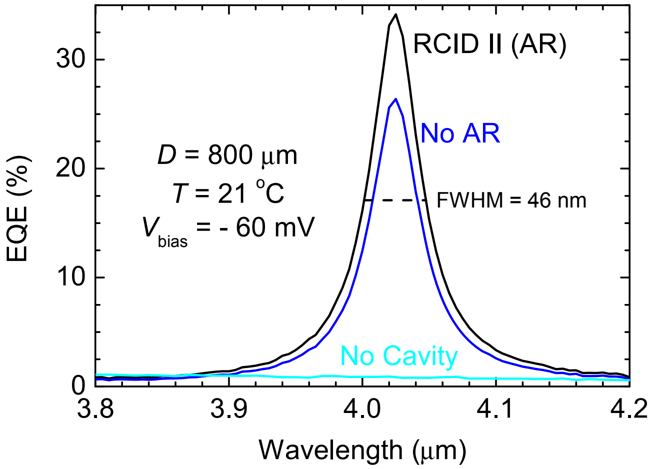

Fig. 7. Quantum efficiency spectra at T = 21 °C for RCID II at an applied bias of −60 mV, before and after an AR coating was deposited on the substrate side. These results are compared to the non-resonant spectrum for a test structure with the same absorber but no cavity (no AR coating).

Figure 8 plots the peak EQEs as a function of reverse bias voltage for devices from all three RCID wafers and the test structure. We find that in all cases a reverse bias of −60 mV is sufficient to bring the peak EQE to within a few percent of its maximum value. This confirms that the diode heterostructure illustrated in Fig. 2 does not impose any significant barriers to the transport and collection of minority carriers. Temperature-dependent measurements confirm that the required bias voltage remains small down to 100 K.

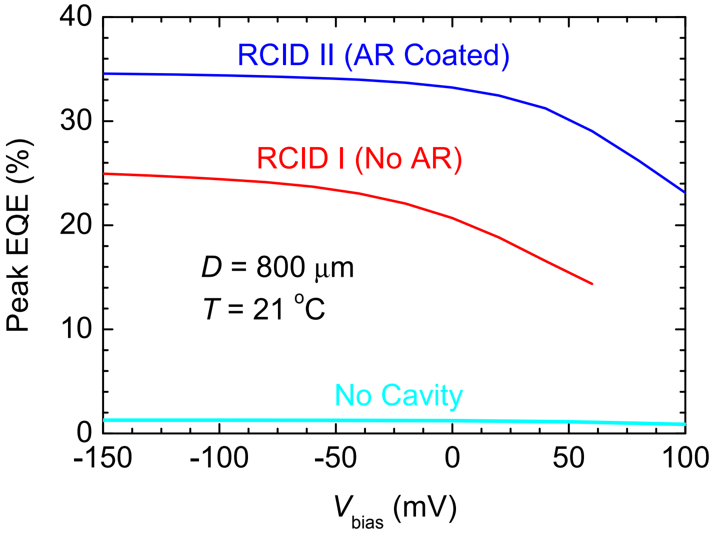

Fig. 8. Dependences of the peak quantum efficiencies on applied bias for devices from both RCID wafers and the test structure.

We see from Figs. 6 and 8 that the resonance enhancement factor, the resonance linewidth, and the dependence of EQE on bias voltage are quite similar for devices processed from both RCID wafers. The only significant difference in performance is the substantial reduction of dark current density that occurred with each successive growth (Fig. 4). This may be attributed to a progressive improvement of the grown material quality with time following a vent.

5. Conclusion

We have demonstrated a resonant cavity infrared photodetector with only 5 absorbing quantum wells that displays a peak quantum efficiency of 34% in a narrow resonance (FWHM = 46 nm) centered at λ_{res} = 4.0 μm. With a resonance enhancement of the external quantum efficiency by nearly a factor of 30, the resulting D^* of 7×10^9 cm $\text{Hz}^{1/2}$/W exceeds all previously reported results for MWIR RCIDs operating at room temperature by at least an order of magnitude. This is the first unequivocal demonstration that multiple passes through a very thin absorber can provide high EQE combined with low dark current density in the MWIR.

We determined that the minority-carrier lifetimes in the absorbing QWs of our present materials is two orders of magnitude shorter than the state-of-the-art values reported for MWIR Ga-free superlattices. This implies that the RCID performance has substantial room for further improvement once thin absorbers with longer lifetimes are inserted into similar resonant cavities. Additional improvements may result from: (1) positioning the absorber more precisely at the antinode of the cavity optical field; (2) further increasing the EQE enhancement at the expense of narrowing the resonance linewidth by adding more periods (> 7) to the Bragg mirror in order to increase its reflectivity; (3) decreasing the number of absorbing quantum wells (to < 5), so as to decrease the dark current density; and (4) increasing the bandgap in the absorber by several hundred nm, which will reduce the dark current with little change in the EQE since the present RCID II device operates at $\lambda_{res} \approx 600$ nm shorter than the bandgap wavelength of ≈4.6 μm. If the minority-carrier lifetime can be improved by two orders of magnitude, we expect an order of magnitude increase in D^* due to that mechanism alone. If a narrower linewidth can be tolerated, D^* may improve by an additional factor of 2, provided only one absorbing well is used in combination with a higher-reflectivity Bragg mirror. The other suggested modifications may contribute more modest, but non-negligible D^* increases.

The RCID approach can also be extended to the LWIR spectral band, using similar Ga-free materials based on InAs/InAsSb superlattices and quantum wells in a photodiode or *nBn* configuration. A further advantage of the RCID configuration is that the extreme thinness of the absorber opens the design space beyond what is normally available to a thicker structure, e.g., by placing the QWs entirely within the depletion region of a *p-n* junction or imposing much higher strain without exceeding the critical thickness [19].

Funding

Defense Advanced Research Projects Agency (DARPA).

References

1. J. Piotrowski and W. Gawron, "Ultimate performance of infrared photodetectors and figure of merit of detector material," Infrared Phys. Technol. **38**(2), 63–68 (1997).
2. R. T. Hinkey and R. Q. Yang, "Theory of multiple-stage interband photovoltaic devices and ultimate performance limit comparison of multiple-stage and single-stage interband infrared photodetectors," J. Appl. Phys. **114**(10), 104506 (2013).
3. A. Rogalski, *Infrared Detectors*, 2nd ed., (CRC Press, 2010).
4. W. E. Tennant, "Interpreting mid-wave infrared (MWIR) HgCdTe photodetectors," Prog. Quantum Electron. **36**(2-3), 273–292 (2012).
5. D. Z. Ting, A. Soibel, A. Khoshakhlagh, S. R. Rafol, S. A. Keo, L. Höglund, A. M. Fisher, E. M. Luong, and S. D. Gunapala, "Mid-wavelength high operating temperature barrier infrared detector and focal plane array," Appl. Phys. Lett. **113**(2), 021101 (2018).
6. L. Höglund, D. Z. Ting, A. Soibel, A. Fisher, A. Khoshakhlagh, C. J. Hill, S. Keo, and S. D. Gunapala, "Minority carrier lifetime in mid-wavelength infrared InAs/InAsSb superlattices: Photon recycling and the role of radiative and Shockley-Read-Hall recombination mechanisms," Appl. Phys. Lett. **105**(19), 193510 (2014).

7. C. C. Chang, Y. D. Sharma, Y. S. Kim, J. A. Bur, R. V. Shenoi, S. Krishna, D. Huang, and S. Y. Lin, "A surface plasmon enhanced infrared photodetector based on InAs quantum dots," Nano Lett. **10**(5), 1704–1709 (2010).
8. E. M. Jackson, J. A. Nolde, M. Kim, C. S. Kim, E. R. Cleveland, C. A. Affouda, C. L. Canedy, I. Vurgaftman, J. R. Meyer, E. H. Aifer, and J. Lorentzen, "Two-dimensional plasmonic grating for increased quantum efficiency in midwave infrared *nBn* detectors with thin absorbers," Opt. Express **26**(11), 13850–13864 (2018).
9. M. S. Ünlü and S. Strite, "Resonant cavity enhanced photonic devices," J. Appl. Phys. **78**(2), 607–639 (1995).
10. A. G. Dentai, R. Kuchibhotla, J. C. Campbell, C. Tsai, and C. Lei, "High quantum efficiency, long wavelength InP/InGaAs microcavity photodiode," Electron. Lett. **27**(23), 2125–2127 (1991).
11. F. Y. Huang, A. Salvador, X. Gui, N. Teraguchi, and H. Morkoc, "Resonant-cavity GaAs/InGaAs/AlAs photodiodes with a periodic absorber structure," Appl. Phys. Lett. **63**(2), 141–143 (1993).
12. N. E. J. Hunt, E. F. Schubert, and G. J. Zydzik, "Resonant-cavity *p-i-n* photodetector utilizing an electron-beam evaporated Si/SiO$_2$ microcavity," Appl. Phys. Lett. **63**(3), 391–393 (1993).
13. M. Böberl, T. Fromherz, T. Schwarzl, G. Springholz, and W. Heiss, "IV–VI resonant-cavity enhanced photodetectors for the mid-infrared," Semicond. Sci. Technol. **19**(12), L115–L117 (2004).
14. J. G. A. Wehner, T. N. Nguyen, J. Antoszewski, C. A. Musca, J. M. Dell, and L. Faraone, "Resonant cavity enhanced mercury cadmium telluride detectors," J. Electron. Mater. **33**(6), 604–608 (2004).
15. A. M. Green, D. G. Gevaux, C. Roberts, and C. C. Phillips, "Resonant-cavity-enhanced photodetectors and LEDs in the mid-infrared," Physica E **20**(3-4), 531–535 (2004).
16. N. Quack, S. Blunier, J. Dual, F. Felder, M. Arnold, and H. Zogg, "Mid-infrared tunable resonant cavity enhanced detectors," Sensors (Basel) **8**(9), 5466–5478 (2008).
17. J. Wang, J. Hu, P. Becla, A. M. Agarwal, and L. C. Kimerling, "Resonant-cavity-enhanced mid-infrared photodetector on a silicon platform," Opt. Express **18**(12), 12890–12896 (2010).
18. T. A. O'Loughlin, G. R. Savich, D. E. Sidor, B. T. Marozas, T. D. Golding, K. D. Jamison, L. Fredin, B. Fowler, W. Priyantha, and G. W. Wicks, "Mid-IR resonant cavity detectors," J. Vac. Sci. Technol. B **35**(2), 02B111 (2017).
19. J. R. Meyer, I. Vurgaftman, C. L. Canedy, W. W. Bewley, C. S. Kim, C. D. Merritt, M. V. Warren, and M. Kim, "Resonant-Cavity Infrared Photodetectors with Fully-Depleted Absorbers," U.S. Patent #10,062,794, 28 August 2018.
20. W. E. Tennant, "Rule 07" revisited: still a good heuristic predictor of p/n HgCdTe photodiode performance?" J. Electron. Mater. **39**(7), 1030–1035 (2010).
21. D. I. Babic and S. W. Corzine, "Analytic expressions for the reflection delay, penetration depth, and absorbance of quarter-wave dielectric mirrors," IEEE J. Quantum Electron. **28**(2), 514–524 (1992).
22. C. L. Canedy, C. S. Kim, M. Kim, D. C. Larrabee, J. A. Nolde, W. W. Bewley, I. Vurgaftman, and J. R. Meyer, "High-Power, Narrow-Ridge, Mid-Infrared Interband Cascade Lasers," J. Vac. Sci. Technol. B **26**(3), 1160–1162 (2008).
23. W. W. Bewley, C. L. Canedy, C. S. Kim, C. D. Merritt, M. V. Warren, I. Vurgaftman, J. R. Meyer, and M. Kim, "Room-temperature Mid-Infrared Interband Cascade Vertical-Cavity Surface-Emitting Laser," Appl. Phys. Lett. **109**(15), 151108 (2016).
24. J. A. Nolde, E. M. Jackson, M. F. Bennett, C. A. Affouda, E. R. Cleveland, C. L. Canedy, I. Vurgaftman, G. G. Jernigan, J. R. Meyer, and E. H. Aifer, "Reticulated Shallow Etch Mesa Isolation for Controlling Surface Leakage in GaSb-Based Infrared Detectors," Appl. Phys. Lett. **111**(5), 051102 (2017).
25. M. P. Lumb, M. Gonzalez, I. Vurgaftman, J. R. Meyer, J. Abell, M. Yakes, R. Hoheisel, J. G. Tischler, P. P. Jenkins, P. N. Stavrinou, M. Fuhrer, N. J. Ekins-Daukes, and R. J. Walters, "Simulation of novel InAlAsSb solar cells," Proc. SPIE **8256**, 82560S (2012).
26. http://www.teledynejudson.com/products/lead-selenide-detectors; https://www.lasercomponents.com/fileadmin/user_upload/home/Datasheets/lcdgp/pbse-pb45-series.pdf.
27. L. Lei, L. Li, H. Lotfi, H. Ye, R. Q. Yang, T. D. Mishima, M. B. Santos, and M. B. Johnson, "Midwavelength interband cascade infrared photodetectors with superlattice absorbers and gain," Opt. Eng. **57**(01), 011006 (2017).